

Colloidal Quantum Dot Solar Cells Exploiting Hierarchical Structuring

André J. Labelle,[†] Susanna M. Thon,^{†,‡} Silvia Masala,^{†,§} Michael M. Adachi,[†] Haopeng Dong,^{†,||} Maryam Farahani,[†] Alexander H. Ip,[†] Andrea Fratalocchi,[§] and Edward H. Sargent^{*,†}

[†]Department of Electrical and Computer Engineering, University of Toronto, 10 King's College Road, Toronto, Ontario M5S 3G4, Canada

[‡]Department of Electrical and Computer Engineering, Johns Hopkins University, Baltimore, Maryland 21218, United States

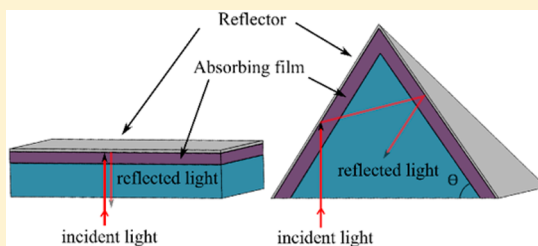
[§]Solar and Photovoltaic Engineering Research Center, King Abdullah University of Science and Technology, 4700 Thuwal 23955-6900, Saudi Arabia

^{||}Key Lab of Organic Optoelectronics and Molecular Engineering of Ministry of Education, Department of Chemistry, Tsinghua University, Beijing, People's Republic of China

S Supporting Information

ABSTRACT: Extremely thin-absorber solar cells offer low materials utilization and simplified manufacture but require improved means to enhance photon absorption in the active layer. Here, we report enhanced-absorption colloidal quantum dot (CQD) solar cells that feature transfer-stamped solution-processed pyramid-shaped electrodes employed in a hierarchically structured device. The pyramids increase, by up to a factor of 2, the external quantum efficiency of the device at absorption-limited wavelengths near the absorber band edge. We show that absorption enhancement can be optimized with increased pyramid angle with an appreciable net improvement in power conversion efficiency, that is, with the gain in current associated with improved absorption and extraction overcoming the smaller fractional decrease in open-circuit voltage associated with increased junction area. We show that the hierarchical combination of micron-scale structured electrodes with nanoscale films provides for an optimized enhancement at absorption-limited wavelengths. We fabricate 54.7° pyramid-patterned electrodes, conformally apply the quantum dot films, and report pyramid CQD solar cells that exhibit a 24% improvement in overall short-circuit current density with champion devices providing a power conversion efficiency of 9.2%.

KEYWORDS: Colloidal quantum dots, photovoltaics, photonically enhanced solar cells, structured substrates



Solution-processed thin film solar cells are attractive for their low-cost fabrication and reduced materials utilization.^{1–9} However, many of these thin-film technologies suffer from the fact that the thickness from which photogenerated charge can be efficiently extracted, their transport length, is less than the worst-case optical absorption length within the medium. This mismatch, commonly termed the absorption-extraction compromise, prevents the efficient utilization of incoming solar photons whose energy exceeds the semiconductor's bandgap ($E_{\text{photon}} > E_{\text{bandgap}}$).^{10–13}

Colloidal quantum dot (CQD) active layers are of interest in solution-processable photovoltaics because of the size-effect tunability of their bandgap. Their transport length today has reached ~ 400 nm^{11,14} but their absorption lengths exceed 1 μ m for infrared, above-bandgap radiation. Once this limitation is addressed, size-tuned CQDs offer the prospect of readily fabricated tandem and multijunction cells to provide improved harvest of the full solar spectrum.^{8,9}

From a materials perspective, CQD solar cells continue to experience global improvement in power conversion efficiency (PCE) owing to improved passivation/interfacing of layers. They have reached greater than 8.5% certified PCE with the aid of electronic materials property improvements such as

improved electronic trap passivation based on halide anions.^{7,15–18} Complementary to these advances, architecture-level strategies have been explored that aim to address the absorption-extraction compromise of CQD films through improved device structure, including the use of bulk heterojunction,¹⁹ depleted bulk heterojunction^{20–24} and scattering-absorption enhancement techniques.^{25–27} So far, bulk heterojunction attempts, which produce a many-fold increase in junction area, have lessened open-circuit voltage (due to increased bimolecular recombination rate at the increased-area interface^{20,28,29}) and have not yet led to net power conversion efficiency advances.^{20,25} Work on nanostructuring for enhanced solar cell performance has been detailed in reviews by Cui,^{30,31} which provide in-depth analyses of photon management techniques for enhanced light utilization for a range of silicon-based photovoltaic technologies. These concepts provide the foundation for development

Received: October 24, 2014

Revised: December 17, 2014

Published: December 30, 2014

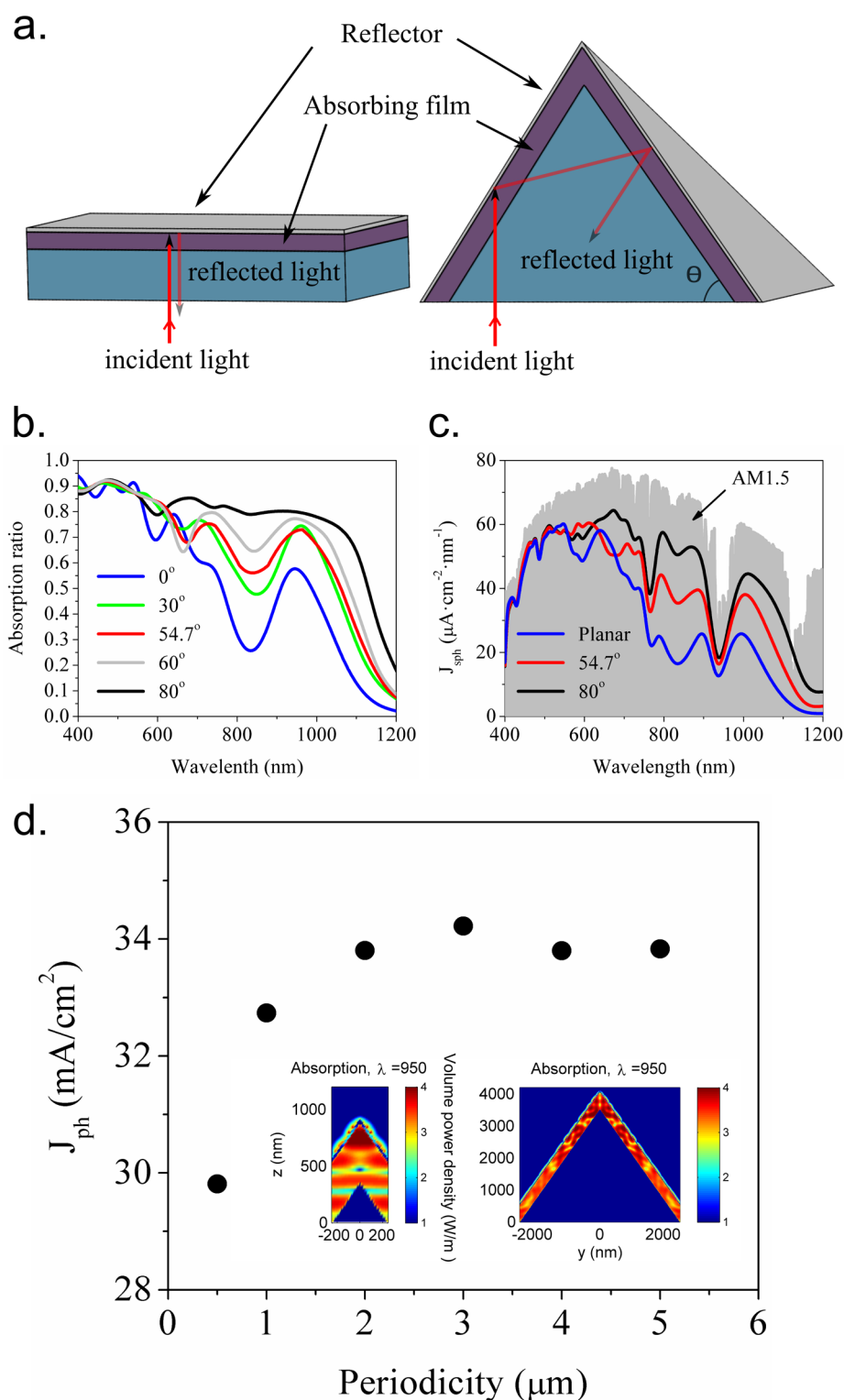


Figure 1. Theoretical predictions of enhanced performance for pyramid-patterned thin-film solar cell. (a) Illustrating the increased-light-path advantage of pyramid-patterned electrodes with detailed equations of the light-film interaction as a function of pyramid angle given in Supporting Information S1. (b) Results of 2D FDTD simulations of absorption as a function of pyramid angle of inclination. Absorption improves most dramatically at wavelengths >600 nm with near complete absorption for the 80° -pyramid case. (c) Projected spectral current-density plotted as a function of wavelength (assuming 100% IQE). (d) Results of 3D FDTD simulations of projected J_{ph} as a function of pyramid pitch. Note that projected current generation is optimized for pitch of $\sim 2 \mu\text{m}$ and this effect saturates for periodicity $> 2 \mu\text{m}$. (Inset left) Absorbed power density map for 500 nm pitch pyramid ($\lambda = 950$ nm). Note standing-wave interference patterns similar to those expected in planar absorption profiles for similar film thicknesses. (Inset right) Absorbed power density map for 5 μm pitch pyramid ($\lambda = 950$ nm). In this case, the absorption is reflective of geometric scattering within the active film for long wavelength radiation ($\lambda = 950$ nm).

of light recycling techniques applied to thin-film technologies, including those presented in this work.

Here we develop a structured electrode which, coupled with conformal CQD film deposition techniques,¹⁴ produces a net performance enhancement in CQD cells. We postulated that an ideal enhancement strategy should employ the best available CQD materials in each sublayer of the active device and should minimize loss in open circuit voltage (V_{oc}) and fill factor (FF) associated with increased junction area. We would require that any added processing steps would be scalable and low in implementation cost.

We fabricated pyramid-shaped transparent electrodes using a simple stamping procedure. We then overcoated the pyramid electrodes conformally using CQD films.¹⁴ With the appropriate selection of periodicity and size, the pyramids give more than a 2-fold improvement in effective absorption length at negligible cost to area and voltage. We term this concept hierarchical structuring, as we exploit three different length scales in our devices. We employ quantum dots that are structured on the few-nanometer length scale ($\sim 3\text{--}5$ nm in diameter, necessary for bandgap tuning), that are assembled into thin films structured on the 100 nm length scale ($\sim 300\text{--}400$ nm thickness, necessary for efficient charge extraction), atop micron length scale pyramids ($\sim 2\text{--}10$ μm , necessary for optimum light collection), thus applying a hierarchy of size-scales for optimal results. The conformally coated stamped pyramids approach ultimately leads to lab-record efficiencies for colloidal quantum dot solar cells. We achieved a 2-fold improvement in external quantum efficiency at absorption-limited wavelengths, leading to an overall 24% improvement in short-circuit current density.

The absorption advantage of this structure relies on in-film scattering from the back electrode and results from the increased light path through the active material (Figure 1a). In a planar device with a reflective top contact, light will pass through the active material twice with a path length of $\sim 2\times$ thickness for normal incidence irradiation. For the pyramid-patterned case, light is trapped within the structure and will reflect internally as a function of pyramid angle with approximately four passes through the active material in the case of 54.7° -pyramids and up to 12 passes for the 80° -pyramids case. The spectral absorption of the CQD film, as a function of thickness, is given by eq 1, where p is the total light path through the active film and $\alpha(\lambda)$ is the spectral absorption coefficient for the CQD material. The length of each pass is further increased by a factor of $1/\cos(\alpha_i)$, wherein the total light path (p) is given by eq 2, where t is the CQD film thickness and m and α_i are defined in more detail in the Supporting Information

$$A(\lambda) = 1 - e^{-\alpha(\lambda)t} \quad (1)$$

$$p = \sum_{i=1}^m \frac{2t}{\cos(\alpha_i)} \quad (2)$$

To determine the quantitative absorption enhancement in a photovoltaic device we performed two-dimensional finite-difference time-domain (FDTD) simulations for the complete layer structure of a depleted heterojunction CQD solar cell, including 300 nm thick, 1.3 eV bandgap lead-sulfide (PbS) CQD films on pyramid-patterned titania (TiO_2) electrodes. The spectral absorption of the quantum dot film is presented as a function of pyramid inclination angle (Figure 1b). We note

significantly increased absorption for pyramid angles that cause additional passes through the CQD film. The most dramatic enhancement occurs for the 80° -pyramid case in which near-complete absorption is expected over the spectral range of interest for this material. FDTD simulations reveal a relative enhancement of more than 50% at the exciton peak (950 nm wavelength) with a maximum enhancement of $\sim 200\%$ at the weakly absorbed (excitonic valley) wavelength of 850 nm. For pyramid angle of 54.7° , there is a relative absorption enhancement of $\sim 100\%$ at this wavelength of 850 nm. We note that absorption is increased for specific critical angles at which extra reflections would occur inside the pyramid-shaped active layer. The trend does not, however, indicate that larger angle leads to increased absorption in all cases. We note that for 30° pyramids, the absorption is in fact slightly higher than for 54.7° . Applying theoretical predictions as detailed in Supporting Information S1 and according to eqs 1 and 2 presented above, we find that p (interaction length of light with active material) is approximately 6.0 times the thickness of the film for the 30° case, while p is 4.8 times the film thickness for 54.7° . Despite this theoretical advantage we chose to work with 54.7° pyramids for practical reasons: silicon's natural etch plane of 54.7° directly facilitates implementation of pyramids exhibiting these sidewall angles.

The spectral photogenerated current-density (J_{sph}) was plotted as a function of wavelength for planar, 54.7° -pyramids and 80° -pyramids. J_{sph} is the current density that would flow if internal quantum efficiency (IQE) were 100%, that is, it is the absorbed photon current. The maximum available current density (assuming 100% absorption of the AM1.5 spectrum) is included for comparison (Figure 1c). Comparing with the planar 300 nm-thick active-layer CQD device, the integrated J_{sph} is predicted to improve by approximately 25% for the 54.7° -pyramids case and nearly 50% for the 80° -pyramids case.

Next, we investigated the impact of angle of inclination on overall power conversion efficiency, taking account of not only photocurrent enhancement but also increased interfacial area and its impact on open-circuit voltage. Further, to add realism and facilitate comparison with experiments, we also used experimentally determined spectra of IQE in estimating the short circuit current (J_{sc}) (Supporting Information S2 and S3). Using optical and electronic parameters for the best previously reported CQD solids, we predicted a power conversion efficiency (PCE) of $\sim 10\%$ for 300 nm-thick PbS CQD films conformally coated atop 80° -pyramids with projected J_{sc} and V_{oc} of 30 mA/cm^2 and 0.56 V, respectively. The PCE for 54.7° -pyramids was predicted to be $\sim 9.2\%$ compared with a predicted PCE of $\sim 7.7\%$ PCE for the planar case.

We then explored whether the in-plane period of pyramid position impacted the optical structural enhancements of interest. We used three-dimensional (3D) FDTD simulations. In Figure 1d, we plot photogenerated current-density (J_{ph}) as a function of pyramid pitch for 54.7° -pyramids. Optimal enhancement in current generation occurs for approximately micron-scale pitch. The improvement as a function of pitch saturates for period > 2 μm in the case of 300 nm thick CQD films. Comparing absorbed power density for a pyramid-pitch of 500 nm versus 5 μm (inset of Figure 1d) we note standing wave interference patterns in the submicron case. Such effects limit the potential for absorption enhancement for longer wavelength radiation (e.g., out to $\lambda = 1000$ nm in the CQD absorber case of interest herein). This effect was observed in other reports investigating the effects of inverted-pyramid pitch

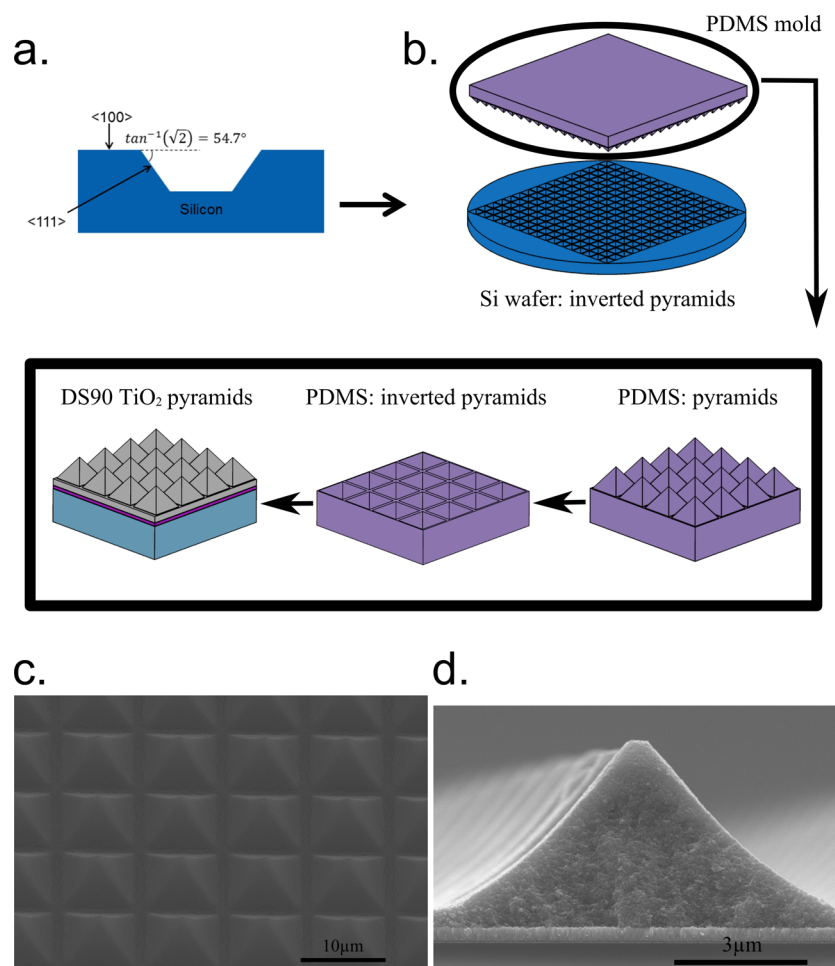


Figure 2. Fabrication of pyramid-patterned titania (TiO_2) electrodes. (a) Illustrating the effects of anisotropic etching on $\langle 100 \rangle$ -oriented silicon. The $\langle 100 \rangle$ plane etches preferentially at a rate 100 \times faster than the $\langle 111 \rangle$ plane, creating inverted pyramid features with angle of 54.7° . (b) Fabrication flow for preparing pyramid-patterned electrodes. The PDMS mold is first prepared using the patterned silicon wafer as a master; a reciprocal PDMS stamp is prepared from this mold to obtain inverted pyramid features. This stamp is then used to pattern the TiO_2 electrode. (c) SEM showing the pyramid-patterned TiO_2 electrode. Pyramid pitch is roughly 9–10 μm with pyramid size of 8–9 μm . (d) Cross-sectional SEM of a single TiO_2 pyramid. Height is estimated to be approximately 5 μm .

on optical reflection for silicon solar cells.^{32,33} As detailed in one of these reports,³³ for wavelengths greater than the period of the pyramids, only a zeroth order wave is present and propagates essentially as a plane wave along the light incidence axis. For $D > 2\lambda$, the system is geometric-optics dominated and transmission through the surface is consequently maximized.³³ In sum, in the case of CQD solar cells, which absorb up to $\lambda \sim 1000$ nm, we thus require $>2 \mu\text{m}$ pitch to ensure we are in a geometric-optics dominated regime which leads to the most optimal degree of light coupling into the film. This limitation necessitates a structuring strategy on the multimicron length-scale. For added ease of fabrication, we selected a periodicity of 10 μm for this study.

We created first a template for pyramids using anisotropic etching of silicon. We applied wet-etch techniques to $\langle 100 \rangle$ -oriented wafers, producing inverted pyramid features with inclination angle of 54.7° (Figure 2a) based on a periodic pattern. These have much in common with the passivated emitter rear locally diffused (PERL) silicon photovoltaic cell,^{34–36} which employ inverted pyramidal structures to reduce reflection at the silicon–air interface. In this work, this concept was deployed for increased light trapping in the active film, an application that would prove unnecessary for silicon as it is

already a complete absorber of above-bandgap photons at typical device thicknesses. We prepared the silicon master using photolithography (see Methods). After silanization treatment³⁷ of the silicon master's patterned surface, we molded polydimethylsiloxane (PDMS) to achieve high-fidelity transfer of pyramid features. A second transfer process was applied to print reciprocal inverted-pyramid structures into PDMS to form the stamp. After applying a thin viscous film of TiO_2 nanoparticle solution on the substrate, the PDMS stamp (with inverted pyramids) was then applied and solvents were allowed to dry (Figure 2b). The result was pyramid-patterned TiO_2 films (Figure 2c,d) with pitch of 10 μm , pyramid base widths of 8–9 μm , and pyramid height of approximately 5 μm .

With conformal PbS CQD films on pyramid-patterned electrodes, we were able to achieve consistent performance improvements over planar controls. Scanning electron microscopy (SEM) images compare CQD films on both planar (Figure 3a) and pyramid-patterned electrodes (Figure 3b). Film thickness was measured to be approximately 350 ± 30 nm for the planar case, and approximately 400 ± 30 nm in the pyramid case; we consider these thicknesses to be in agreement taking into account the considerable experimental uncertainty of these measurements. Total absorption (including absorption of FTO

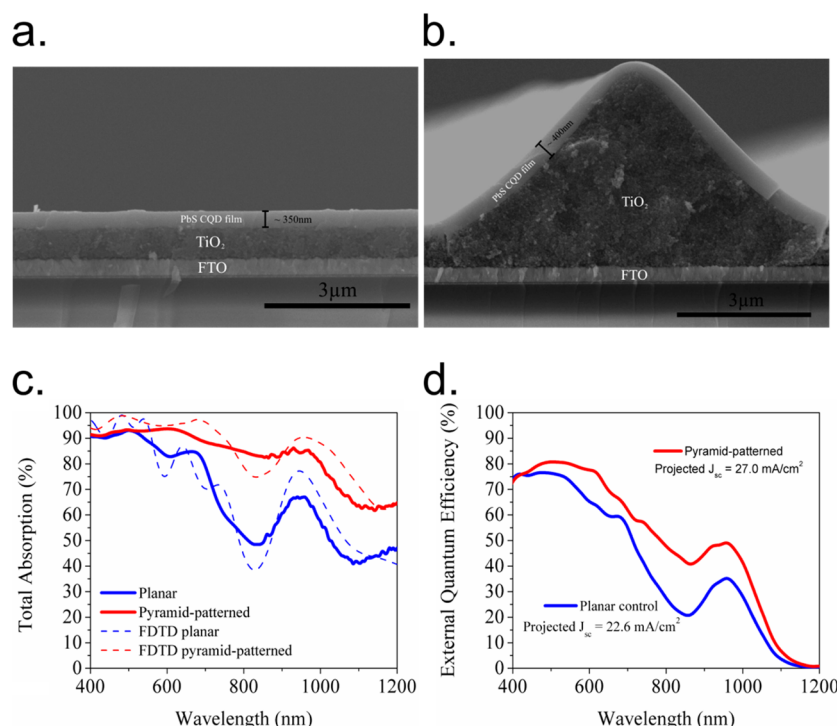


Figure 3. Enhanced absorption and quantum efficiency for pyramid-patterned CQD solar cell. (a) Cross-sectional SEM of planar CQD device. The film thickness is $\sim 350 \pm 30$ nm. (b) Cross-sectional SEM of a pyramid-patterned CQD device. The film thickness is $\sim 400 \pm 30$ nm. (c) Total absorption (including absorption of FTO and top contact materials) of pyramid-patterned device compared to planar control. There is increased absorption at wavelengths >600 nm for the structured device, and excellent agreement with 2D FDTD simulation data for both samples. (d) External quantum efficiency (EQE) of a pyramid-patterned sample versus a planar control. The EQE response is most improved for the wavelength range between 700 and 1000 nm with $\sim 100\%$ improvement at 850 nm over the planar control.

and top contact) is compared for both samples (Figure 3c). Results are in excellent agreement with simulated (2D FDTD) spectra of total absorption (for 54.7° pyramids and 300 nm-thick PbS films) with significantly improved absorption at wavelengths >600 nm for the pyramid-patterned sample. In the most dramatic case, total absorption is improved by $\sim 72\%$ for the pyramid-patterned case at weakly absorbed wavelengths ($\lambda = 830$ nm). We note the presence of additional peaks in the simulated absorption plots that arise from thin film interference effects. However, for the experimentally built pyramids we find that the somewhat curved peaks and valleys, and their slightly rough sidewalls, produce an effective spectral averaging that diminishes these sharp resonances. A similar effect is observed for planar devices that are built atop rough fluorine-doped tin oxide films.

External quantum efficiency (EQE) of pyramid-patterned and planar control samples was also compared (Figure 3d). The predicted J_{sc} from measured EQE agreed well, to within 5%, with measured values of J_{sc} under AM1.5 illumination. We observe a substantial enhancement of EQE in the infrared spectral region for the structured sample with $\sim 100\%$ enhancement at $\lambda \sim 850$ nm, indicative that improved device performance is the result of increased light path through the active layer, as indicated by absorption measurements.

Current density–voltage (J – V) characteristics for the record pyramid-patterned device were also compared with the best planar control (Figure 4a). We obtained a power conversion efficiency of 9.2%, matching a lab-record for colloidal quantum dot solar cells. This represents an enhancement of 15% in PCE over the best planar control with an overall improvement of $\sim 24\%$ in J_{sc} . Open-circuit voltage and fill-factor were

comparable (to within experimental uncertainty) for the two devices. Thus, conformal films preserve the FF in the structured case, and any loss in V_{oc} is minimal, as projected (<0.02 V) for 54.7° pyramids. As expected from theoretical treatments and quantum efficiency measurements, the pyramid-patterned device generates additional photocurrent from increased absorption inside the same thickness of active material (perpendicular to the electron-accepting electrode). As discussed, the limited charge transport of CQD films dictates that the most efficient thickness for transport is too thin to achieve complete absorption of incident radiation. The pyramids effectively enhance absorption in the active film without increasing the electrode-to-electrode distance, and they do so by increasing both the angle of transmission through the active layer, and the number of optical passes in the device: 4–6 effective passes occur in the pyramid devices compared to the 2 that occur in a planar device.

To characterize reproducibility, we plotted all device results over a one month period (with optimized stamping and film fabrication procedures) in a histogram. For a sample size of 126 pyramid-patterned devices (i.e., 126 individual devices as defined by the 0.049 cm² contact area) prepared with similar substrate stamping and film fabrication protocols, we report an average power conversion efficiency of 8.2% with a standard deviation of $\pm 0.6\%$. For comparison, the average device performance for a sample size of 124 planar devices (also defined as 124 individual 0.049 cm² devices) is $6.5 \pm 0.8\%$.

As demonstrated in this study, there exists potential for additional absorption enhancement when using steeper-angle pyramids. The good agreement between experiment and theory herein suggests that the 80° pyramids could indeed enable

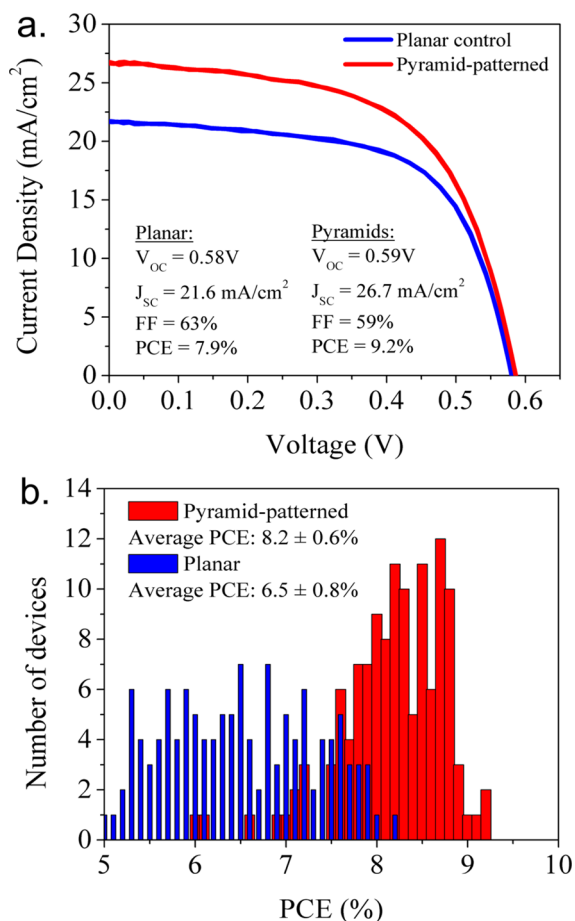


Figure 4. Enhanced performance of pyramid-patterned CQD thin-film solar cell. (a) J - V curve comparing device performance of a pyramid-patterned sample versus a planar control. PCE was measured as 9.2% for the pyramid-patterned sample, a 15% improvement over the planar control. (b) Histogram of pyramid-patterned CQD device performance over a one month period (red) and planar control device performance (blue). Average PCE of $8.2 \pm 0.6\%$ was computed for a sample size of 126 pyramid-patterned samples. Comparatively, the lab-wide average (neglecting outliers) for planar CQD devices was $6.5 \pm 0.8\%$ for a sample size of 124.

devices that reach above 10% solar PCE. These structures could further be adapted to other thin-film technologies or alternative CQD-based films for comparable absorption enhancement and subsequent current generation benefits with minimal losses in open-circuit voltage and fill-factor.

In summary, we made use of a structured substrate for increased absorption in transport-limited CQD films and applied conformal absorbing films to leverage the full potential of the structured design. Using micron-scale pyramid features as part of a hierarchical structured device, we achieved 9.2% solar PCE as a result of a 24% improvement in J_{sc} over the planar control. When statistics were gathered for over 100 devices, we achieved a 26% improvement in the mean pyramid device relative to the mean planar control.

Methods. Finite-Difference Time-Domain Simulations. Finite-difference time-domain simulations were carried out using Lumerical FDTD Solutions software (<http://www.Lumerical.com>) version 8.7.4. The 2D simulations were for pyramid (with periodicity, size, and side-wall angle as defined in the text) or planar structures at the midline along the z -axis with periodic boundary conditions in the x -direction. The 3D

simulations were for pyramid (with periodicity, size, and side-wall angle as defined in the text) or planar structures with periodic boundary conditions in the x - and y -directions. A broadband ($\lambda = 400$ – 1200 nm) planewave source polarized along the y -axis was incident from within the glass region. The absorption was isolated for the individual layers and only the absorption of the CQD layer is presented in Figure 1, while Figure 3 represents the total absorption of all active layers in the device. Note that photogenerated current density (J_{ph}) presented in Figure 1d was computed assuming an internal quantum efficiency of 100% and integrating the predicted absorption curve against the AM1.5 solar irradiance spectrum.

Silicon Master Preparation. The silicon (Si) master was prepared from a 4 in. diameter $\langle 100 \rangle$ -oriented silicon wafer coated with 100 nm of PECVD-deposited Si_3N_4 . A grid pattern (with 10 μ m pitch) was transferred to the Si_3N_4 layer via a positive photolithography process. The wafer was then heated at 115 °C for 1 min to evaporate residual surface moisture. An adhesion-promoter, hexamethyldisilazane (HMDS), was spin-cast onto the wafer at 4000 rpm (2500 rpm/s acceleration) for 40 s to promote adhesion between the photoresist and the wafer. S1811 photoresist was then spin-cast onto the substrate at 4000 rpm (2500 rpm/s acceleration) for 90 s. The wafer was then baked at 115 °C for 1 min and exposed to 930W UV radiation for 7.1 s in hard contact mode. The photoresist contained within the 9 μ m \times 9 μ m squares (between grid lines) was developed in MF321 for 28 s and the remaining photoresist covering the 1 μ m wide grid lines was hard-baked at 115 °C for 20 min. The Si_3N_4 was then removed from the 9 μ m \times 9 μ m square-regions (between grid-lines) by reactive ion etching (RIE) in CF_4/CHF_3 (CF_4/CHF_3 , 20 sccm; pressure, 16 mTorr; power, 90 W) for 5 min. The remaining photoresist was removed with a 10 min exposure to acetone. The silicon wafer with Si_3N_4 hard mask was then dipped in 20% KOH in isopropanol at 70 °C, etching the silicon at a rate of 1 μ m/min. The Si_3N_4 hard-mask was then removed with buffered oxide etch (BOE) thus producing a silicon wafer with a periodic array of inverted pyramid features with pitch of 10 μ m and individual pyramid width of 9 μ m.

Electrode Preparation. Polydimethylsilane (PDMS) stamps were prepared using the silicon wafer as a master. Prior to molding the PDMS, the Si surface was treated using a silanization process in which the wafer was treated with an O_2 plasma-etch at 50 W for 5 min (Unitronics PE-25-JW Plasma Cleaning System), then submerged in 30% H_2O_2 to functionalize the surface for silanization exposure. The wafer was then loaded into a glovebox antechamber and exposed to 100 μ L of trichloro-(perfluorooctyl)-silane under low vacuum. PDMS (mixed in a 10:1 ratio of resin:curing agent) was poured over the Si master and heated on a hot plate for 20 min at 125 °C. The PDMS stamp was then used to mold a reciprocal PDMS stamp to be used for preparing the pyramid-patterned electrodes. The silanization process was repeated for the original PDMS mold, and 5 mL of PDMS (10:1 ratio) was poured over the original PDMS mold and treated in an oven for 1 h at 70 °C. The reciprocal PDMS stamp (with inverted pyramid features) was then used to structure the TiO_2 electrode.

TiO_2 Electrode Stamping. Two hundred microliters of viscous TiO_2 solution (1:2 Dyesol DS90 TiO_2 nanoparticles/ethanol) was spin-cast onto an FTO-coated glass substrate at 1000 rpm for 10 s. The PDMS reciprocal stamp was then placed onto the substrate, applying no additional pressure. The

TiO₂ paste was allowed to dry for a minimum of 8 h and the stamp was removed, leaving behind a pyramid-structured TiO₂ film. The substrate was then heat-treated at temperatures of 200, 300, and 400 °C for 15 min each to burn off excess organics from the film. The TiO₂ electrode was then treated with titanium tetrachloride solution; the substrates were submerged in a 120 mM solution of TiCl₄ in deionized water and heated in an oven for 30 min at 70 °C. Substrates were then removed from the oven, rinsed with water, dried with compressed N₂, and heated to 400 °C on a hot plate for 1 h.

Device Fabrication. All devices (pyramid-patterned and planar controls) were prepared using sequential dip-coating. Samples were automatically manipulated using a medium-sized KSV NIMA multivessel dip-coater. The samples were first dipped into 30 mL beakers containing 15 mL of 0.05% mercaptopropionic acid (MPA) in methanol for 5 s, then left to dry for 360 s (surface primer treatment). Samples were then dipped into an adjacent 30 mL beaker containing 15 mL of 7.5 mg/mL PbS quantum dots (synthesized and exchanged following previously published protocols⁷) in hexane for 30 s, and left to dry for 240 s. Samples were then dipped into a 50 mL beaker containing 25 mL of 0.2% MPA in methanol solution (solid-state exchange) for 3 s followed by 60 s drying. Finally, the samples were rinsed in a 50 mL beaker containing 25 mL of pure methanol for 5 s and dried for 120 s. This process was repeated for 10–12 cycles for optimal results. The top contacts were deposited via thermal (molybdenum trioxide and silver) and e-beam (gold) evaporation with a total thickness of 30 nm MoO₃, 50 nm Au, and 200 nm Ag.

Absorption Measurements. The procedure used for these measurements is identical to that published by Adachi et al.²⁵ All absorption measurements were done using a Perkin Elmer Lambda 950 UV–vis–NIR spectrophotometer equipped with an integrating sphere. Samples were placed at the center of the integrated sphere tilted at an angle of 20° relative to the incident beam. The total transmission (*T*) and reflectance (*R*) was collected by the integrating sphere detector with all ports closed except the one for the incident beam. Absorption was calculated as 100% – *T* – *R*. The 100% transmission baseline measurement was an empty sphere.

AM1.5 Photovoltaic Device Characterization. The procedure used for these measurements is similar to that published by Adachi et al.²⁵ All photovoltaic and EQE measurements were carried out under N₂-flow. Current density–voltage curves were measured using a Keithley 2400 source meter with illumination from a Sciencetech solar simulator with an irradiance of 100 mW/cm². The active area of the solar cell was illuminated through a circular aperture with an area of 0.049 cm². The power was measured using a Melles-Griot broadband power meter. The spectral mismatch between measured and actual solar spectra was measured using a calibrated reference solar cell from Newport. A total spectral mismatch of ~4% was taken into account by applying a multiplicative factor of 0.96 to measured current density values. The uncertainty of AM1.5 measurements was estimated to be ±7%.

External Quantum Efficiency Measurements. The procedure used for these measurements is identical to that published by Adachi et al.²⁵ External quantum efficiency spectra were measured under monochromatic light (400 W xenon lamp source passing through a monochromator with order-sorting filters) that was chopped at 220 Hz. A constant 1-sun intensity white-light source simultaneously illuminated the device during

measurements. The monochromatic light power was measured using Newport 818-UV and Newport 818-IR power meters. The current response was measured using a Stanford Research Systems lock-in amplifier at short-circuit conditions. The uncertainty of the EQE measurements, calculated from taking the root-mean-square of the error from all equipment, was ±3%.

■ ASSOCIATED CONTENT

■ Supporting Information

Calculations of path length of light through the active film as a function of pyramid angle, empirically obtained internal quantum efficiency (IQE) of PbS CQD film (300 nm in thickness), evolution of *V_{oc}*, *J_{sc}*, and PCE (using empirical IQE and theoretical absorption) as a function of pyramid angle. This material is available free of charge via the Internet at <http://pubs.acs.org>.

■ AUTHOR INFORMATION

Corresponding Author

*E-mail: ted.sargent@utoronto.ca.

Author Contributions

A.L., S.M.T., and E.H.S. designed this study. S.M. prepared the silicon master. A.L. and H.D. optimized the substrate preparation protocol. A.L. carried out all device fabrication and characterization with assistance from A.I., A.L., M.F., and M.A. performed optical simulations. A.L. wrote the manuscript with comments and feedback from E.H.S. and S.M.T.

Notes

The authors declare no competing financial interest.

■ ACKNOWLEDGMENTS

This publication is based in part on work supported by Award KUS-11-009-21, made by King Abdullah University of Science and Technology (KAUST), by the Ontario Research Fund - Research Excellence Program, and by the Natural Sciences and Engineering Research Council (NSERC) of Canada. We thank Angstrom Engineering, Inc. and Innovative Technology, Inc. for useful discussions regarding material deposition methods and control of the glovebox environment, respectively. H.D. would like to acknowledge financial support from China Scholarship Council (CSC). The authors thank Larissa Levina for the assistance of CQDs synthesis and E. Palmiano, R. Wolowiec, G. Koleilat, and D. Kopilovic for their technical help over the course of this study. We also thank Professor Hernan Miguez of the Institute of Materials Science of Seville for very helpful discussions regarding electrode structuring. We would finally like to thank Professor Peter Herman and Dr. Kitty Kumar, both of the Electrical and Computer Engineering Department at the University of Toronto, for materials and assistance in preparing the Silicon master.

■ REFERENCES

- (1) Mitzi, D. B.; Yuan, M.; Liu, W.; Kellock, A. J.; Chey, S. J.; Deline, V.; Schrott, A. G. *Adv. Mater.* **2008**, *20*, 3657–3662.
- (2) Todorov, T. K.; Reuter, K. B.; Mitzi, D. B. *Adv. Mater.* **2010**, *22*, E156–E159.
- (3) Todorov, T. K.; Tang, J.; Bag, S.; Gunawan, O.; Gokmen, T.; Zhu, Y.; Mitzi, D. B. *Adv. Energy Mater.* **2013**, *3*, 34–38.
- (4) You, J.; Dou, L.; Yoshimura, K.; Kato, T.; Ohya, K.; Moriarty, T.; Emery, K.; Chen, C.-C.; Gao, J.; Li, G.; Yang, Y. *Nat. Commun.* **2013**, *4*, 1446.

- (5) Kaltenbrunner, M.; White, M. S.; Glowacki, E. D.; Sekitani, T.; Someya, T.; Sariciftci, N. S.; Bauer, S. *Nat. Commun.* **2012**, *3*, 770.
- (6) He, Z.; Zhong, C.; Su, S.; Xu, M.; Wu, H.; Cao, Y. *Nat. Photonics* **2012**, *6*, 591–595.
- (7) Ip, A. H.; Thon, S. M.; Hoogland, S.; Voznyy, O.; Zhitomirsky, D.; Debnath, R.; Levina, L.; Rollny, L. R.; Carey, G. H.; Fischer, A.; Kemp, K. W.; Kramer, I. J.; Ning, Z.; Labelle, A. J.; Chou, K. W.; Amassian, A.; Sargent, E. H. *Nat. Nanotechnol.* **2012**, *7*, 577–582.
- (8) Wang, X.; Koleilat, G. I.; Tang, J.; Liu, H.; Kramer, I. J.; Debnath, R.; Brzozowski, L.; Barkhouse, D. A. R.; Levina, L.; Hoogland, S.; Sargent, E. H. *Nat. Photonics* **2011**, *5*, 480–484.
- (9) Choi, J. J.; Wenger, W. N.; Hoffman, R. S.; Lim, Y.-F.; Luria, J.; Jasieniak, J.; Marohn, J. A.; Hanrath, T. *Adv. Mater.* **2011**, *23*, 3144–3148.
- (10) Clifford, J. P.; Konstantatos, G.; Johnston, K. W.; Hoogland, S.; Levina, L.; Sargent, E. H. *Nat. Nanotechnol.* **2009**, *4*, 40–44.
- (11) Zhitomirsky, D.; Voznyy, O.; Hoogland, S.; Sargent, E. H. *ACS Nano* **2013**, *7*, 5282–5290.
- (12) Tress, W.; Corvers, S.; Leo, K.; Riede, M. *Adv. Energy Mater.* **2013**, *3*, 873–880.
- (13) Tress, W.; Merten, A.; Furno, M.; Hein, M.; Leo, K.; Riede, M. *Adv. Energy Mater.* **2013**, *3*, 631–638.
- (14) Labelle, A. J.; Thon, S. M.; Kim, J. Y.; Lan, X.; Zhitomirsky, D.; Kemp, K. W.; Sargent, E. H. *Adv. Mater.*; DOI: adma.201404887.
- (15) Tang, J.; Kemp, K. W.; Hoogland, S.; Jeong, K. S.; Liu, H.; Levina, L.; Furukawa, M.; Wang, X.; Debnath, R.; Cha, D.; Chou, K. W.; Fischer, A.; Amassian, A.; Asbury, J. B.; Sargent, E. H. *Nat. Mater.* **2011**, *10*, 765–771.
- (16) Ning, Z.; Ren, Y.; Hoogland, S.; Voznyy, O.; Levina, L.; Stadler, P.; Lan, X.; Zhitomirsky, D.; Sargent, E. H. *Adv. Mater.* **2012**, *24*, 6295–6299.
- (17) Ning, Z.; Voznyy, O.; Pan, J.; Hoogland, S.; Adinolfi, V.; Xu, J.; Li, M.; Kirmani, A. R.; Sun, J.-P.; Minor, J.; Kemp, K. W.; Dong, H.; Rollny, L.; Labelle, A.; Carey, G.; Sutherland, B.; Hill, I.; Amassian, A.; Liu, H.; Tang, J.; Bakr, O. M.; Sargent, E. H. *Nat. Mater.* **2014**, *13*, 822–828.
- (18) Chuang, C.-H. M.; Brown, P. R.; Bulović, V.; Bawendi, M. G. *Nat. Mater.* **2014**, *13*, 796–801.
- (19) Rath, A. K.; Bernechea, M.; Martinez, L.; de Arquer, F. P. G.; Osmond, J.; Konstantatos, G. *Nat. Photonics* **2012**, *6*, 529–534.
- (20) Barkhouse, D. A. R.; Debnath, R.; Kramer, I. J.; Zhitomirsky, D.; Pattantyus-Abraham, A. G.; Levina, L.; Etgar, L.; Grätzel, M.; Sargent, E. H. *Adv. Mater.* **2011**, *23*, 3134–3138.
- (21) Kramer, I. J.; Zhitomirsky, D.; Bass, J. D.; Rice, P. M.; Topuria, T.; Krupp, L.; Thon, S. M.; Ip, A. H.; Debnath, R.; Kim, H.-C.; Sargent, E. H. *Adv. Mater.* **2012**, *24*, 2315–2319.
- (22) Lan, X.; Bai, J.; Masala, S.; Thon, S. M.; Ren, Y.; Kramer, I. J.; Hoogland, S.; Simchi, A.; Koleilat, G. I.; Paz-Soldan, D.; Ning, Z.; Labelle, A. J.; Kim, J. Y.; Jabbour, G.; Sargent, E. H. *Adv. Mater.* **2013**, *25*, 1769–1773.
- (23) Jean, J.; Chang, S.; Brown, P. R.; Cheng, J. J.; Rekemeyer, P. H.; Bawendi, M. G.; Gradečak, S.; Bulović, V. *Adv. Mater.* **2013**, *25*, 2790–2796.
- (24) Wang, H.; Kubo, T.; Nakazaki, J.; Kinoshita, T.; Segawa, H. *J. Phys. Chem. Lett.* **2013**, *4*, 2455–2460.
- (25) Adachi, M. M.; Labelle, A. J.; Thon, S. M.; Lan, X.; Hoogland, S.; Sargent, E. H. *Sci. Rep.* **2013**, *3*, 2928.
- (26) Koleilat, G. I.; Kramer, I. J.; Wong, C. T. O.; Thon, S. M.; Labelle, A. J.; Hoogland, S.; Sargent, E. H. *Sci. Rep.* **2013**, *3*, 2166.
- (27) Lopez-Lopez, C.; Colodrero, S.; Calvo, M. E.; Miguez, H. *Energy Environ. Sci.* **2013**, *6*, 1260–1266.
- (28) Kemp, K. W.; Labelle, A. J.; Thon, S. M.; Ip, A. H.; Kramer, I. J.; Hoogland, S.; Sargent, E. H. *Adv. Energy Mater.* **2013**, *3*, 917–922.
- (29) Widmer, J.; Tietze, M.; Leo, K.; Riede, M. *Adv. Funct. Mater.* **2013**, *23*, 5814–5821.
- (30) Zhu, J.; Yu, Z.; Fan, S.; Cui, Y. *IEEE Int. Nanoelectron. Conf., 3rd* **2010**, *70*, 330–340.
- (31) Narasimhan, V. K.; Cui, Y. *Nanophotonics* **2013**, *2*, 187–210.
- (32) Han, Y.; Yu, X.; Wang, D.; Yang, D. J. *Nanomater.* **2013**, *2013*, 7–7.
- (33) Llopis, F.; Tobías, I. *Prog. Photovoltaics* **2005**, *13*, 27–36.
- (34) Campbell, P.; Green, M. A. *J. Appl. Phys.* **1987**, *62*, 243–249.
- (35) Zhao, J.; Wang, A.; Altermatt, P. P.; Wenham, S. R.; Green, M. A. *Sol. Energy Mater. Sol. Cells* **1996**, *41–42*, 87–99.
- (36) Campbell, P.; Green, M. A. *PVSEC 11 Part I* **2001**, *65*, 369–375.
- (37) Xia, Y.; Whitesides, G. M. *Angew. Chem., Int. Ed.* **1998**, *37*, 550–575.